

Deep Image Harmonization by Bridging the Reality Gap

Wenyan Cong¹, Junyan Cao², Li Niu^{1*}, Jianfu Zhang¹, Xuesong Gao³, Zhiwei Tang³, Liqing Zhang¹

¹ MoE Key Lab of Artificial Intelligence, Shanghai Jiao Tong University

² Shandong University

³ Hisense Group Holdings Co., Ltd.

¹{plcwyam17320, ustcnewly, c.sis}@sjtu.edu.cn ²junyanc@mail.sdu.edu.cn

³{gaoxuesong, tangzhiwei1}@hisense.com ¹zhang-lq@cs.sjtu.edu.cn

Abstract

Image harmonization has been significantly advanced with large-scale harmonization dataset. However, the current way to build dataset is still labor-intensive, which adversely affects the extendability of dataset. To address this problem, we propose to construct a large-scale rendered harmonization dataset RHHarmony with fewer human efforts to augment the existing real-world dataset. To leverage both real-world images and rendered images, we propose a **Cross-domain harmonization network** CharmNet to bridge the domain gap between two domains. Moreover, we also employ well-designed style classifiers and losses to facilitate cross-domain knowledge transfer. Extensive experiments demonstrate the potential of using rendered images for image harmonization and the effectiveness of our proposed network.

1. Introduction

Image composition is the technique of combining foreground from one image and background from another image into one composite image. However, due to the appearance discrepancy caused by different capture conditions (e.g. weather, season, time of the day) of foreground and background, the quality of composite image might be significantly degraded. Image harmonization aims to diminish the discrepancy by adjusting the appearance of the composite foreground according to the background. Recently, many deep learning based harmonization methods [6, 7, 16, 30, 37] have achieved promising results.

Deep learning based methods require a large-scale training set that contains pairs of composite images and corresponding harmonized results. However, manually creating harmonized results for composite images is highly time-consuming and labor-intensive, making it infeasible to collect abundant training pairs. To address the scarcity

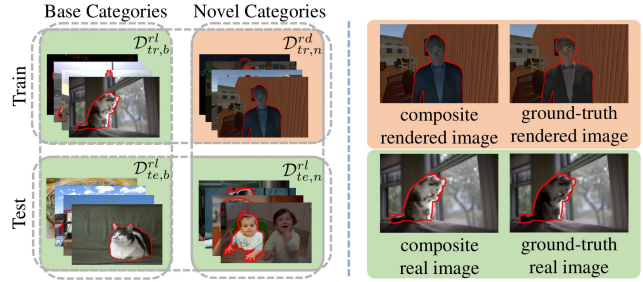


Figure 1: Left sub-figure: illustration of training and test images from base categories and novel categories. Right sub-figure: image pairs from rendered image domain and real image domain. Images in orange (resp., green) are from rendered (resp., real) image domain. The foregrounds are highlighted with red border lines.

of training dataset, Tsai [37] and Cong [6] adopted an inverse approach to construct harmonization dataset, and the first large-scale image harmonization dataset *iHarmony4* [6] was released. Specifically, they take real images as the ground-truth and adjust foreground appearance to generate synthetic composite images, leading to pairs of composite images and ground-truth images.

Though the above data acquisition process is inspiring and feasible in implementation, it requires manually segmenting foregrounds and manually filtering out the composite images which do not satisfy the stringent requirements (e.g. no corruption, unchanged hue) mentioned in [6]. The heavy manual labor hinders the extendability of harmonization dataset. For example, the foreground category (e.g., panda, human) of test composite images may be out of the scope of training set and we observe that cross-category harmonization suffers from a performance drop (see Section 5.3). However, extending the dataset to include novel foreground categories requires heavy human efforts. In the remainder of this paper, the category of a composite image means the category of its foreground to be harmonized.

In this work, we propose to construct image harmoniza-

*Corresponding author.

tion dataset using 3D rendering techniques, which can escape from heavy manual efforts and supplement existing real-world harmonization dataset. Specifically, we utilize 3D rendering software *Unity3D* [35] to generate rendered 2D scenes. By leveraging weather system plugin *Unistorm*, it is convenient to generate a group of images with different capture conditions for each 2D scene. Besides, it is effortless to obtain accurate foreground masks in *Unity3D*. Then, by exchanging the foregrounds within a group of images from the same scene, we could easily obtain abundant pairs of composite rendered images and ground-truth rendered images. The above process is illustrated in Figure 2, and more details will be described in Section 3.

Suppose that existing real-world (“real” for short) dataset (*e.g.*, iHarmony4) has real images with foregrounds from base categories; we can enrich this dataset using rendered images with foregrounds from novel categories. Then, as illustrated in Figure 1, the image harmonization model could be trained on the combination of rendered images and real images, and tested on real images from both base and novel categories. This is a practical setting where our target is enhancing the performance on novel categories that are out of the scope of existing real dataset. In this paper, we take “human” as an example novel category because human harmonization is rather challenging due to large intra-category variance and of paramount interest for many applications (*e.g.*, augmented reality) [33, 41]. So we contribute a Rendered Human Harmonization dataset *RHHarmony*. Notably, our dataset could be easily extended to other novel categories in the same way, which will be explored in the future study.

However, models trained on rendered images (source domain) would suffer from a performance drop when applied to real images (target domain) (see Section 5.3), owing to considerably different data distributions between two domains, which is typically known as domain gap [36, 43]. Hence, we propose a novel **Cross-domain harmonization** Network CharmNet to align two domains when training with a mixture of real images and rendered images. Our CharmNet has three stages, including a domain-specific encoding stage, a domain-invariant encoding-decoding stage, and a domain-specific decoding stage. The first stage projects data from both domains to the same shared domain, where the projected features of two domains are further aligned with an adversarial loss. Then, the second stage encourages information sharing between real images and rendered images. The final stage projects the domain-invariant features back to different domains by enforcing the features to reconstruct the ground-truth images in each domain.

Besides, by naming different capture conditions (*e.g.*, weather, season, time of the day) as different “styles”, we can easily obtain the style labels of rendered images because their capture conditions are controllable using *Unis-*

torm. Therefore, we can exploit such information to facilitate cross-domain knowledge transfer. We assume that the input features before the second stage are inharmonious and the output features after the second stage are harmonious, so that the harmonization process is shared across two domains and more useful information can be transferred from rendered image domain to real image domain. For rendered images, their style labels before and after harmonization are readily available, which could be used to supervise style classification. For real images, their style labels before and after harmonization are unknown, but we assume the style distribution should become more concentrated after harmonization because the foreground style is adapted to the background style. So we propose a novel Style Aggregation (SA) loss to enforce the style distribution to be more concentrated after harmonization. To verify the effectiveness of our proposed network, we conduct comprehensive experiments on real dataset iHarmony4 and our contributed rendered dataset RHHarmony.

Our contributions are summarized as follows: 1) We contribute the first large-scale rendered human harmonization dataset RHHarmony, which contains pairs of composite rendered images and ground-truth rendered images; 2) We propose the first cross-domain image harmonization network CharmNet using both rendered images and real images, with a novel network architecture and a novel style aggregation loss; 3) Extensive experiments on iHarmony4 and RHHarmony datasets demonstrate the potential of using rendered images for image harmonization and the effectiveness of our proposed network.

2. Related Works

2.1. Image Harmonization

Image harmonization has drawn increasing attention in the field of computer vision. Early works [4, 20, 22, 27–29, 32, 34, 42] mainly focused on manipulating the low-level image statistics, such as matching color distributions [28, 29], applying gradient-domain compositing [20, 27, 34], and mapping multi-scale statistics [32]. Recently, thanks to the inspiring data acquisition approach [37], deep learning based methods spring up rapidly. In [30, 37], they both leveraged auxiliary semantic features to improve the basic image harmonization network. In [6], Cong released the first large-scale image harmonization dataset iHarmony4 and introduced a domain verification discriminator pulling close the foreground domain and background domain. In [7, 16], they explored various attention mechanisms for image harmonization. Different from existing methods only using real images, we are the first to use both real images and rendered images to train a cross-domain image harmonization model.

2.2. Domain Adaptation

Domain adaptation strives to reduce the distribution mismatch and make the model trained on source domain generalize well to target domain. In our task, real images and rendered images are treated as two domains. Domain adaptation has been studied in a wide range of applications like classification [12–15], detection [1, 2, 18, 21], segmentation [12, 39, 43, 46], person re-identification [8, 9, 40], and pose estimation [31, 44]. In the above applications, the label/output spaces (*e.g.*, class label, segmentation mask) are the same between two domains. However, in image harmonization, the input and output spaces are the same in each domain but different across domains. Therefore, previous domain adaptation methods cannot be directly applied to our task. To the best of our knowledge, we are the first to address such a challenging task in the realm of domain adaptation.

Another possible domain adaptation approach is to translate images from the source domain to the target domain using Image-to-Image (I2I) translation methods [3, 17, 19, 23–26, 45], so that the translated images can be used for any downstream tasks. Nevertheless, during experiments, we observe that I2I translation methods have poor performance when translating rendered images to real images because they severely distort the illumination statistics. Therefore, I2I translation methods are ill-suited for our task.

3. Dataset Construction

As mentioned in Section 1, we take “human” as the novel category and construct rendered human harmonization dataset RHHarmony, which contains rendered images with human foregrounds. The whole process can be divided into two steps: ground-truth rendered image generation and composite rendered image generation.

3.1. Ground-truth Rendered Image Generation

Generating a large number of rendered images with human foregrounds requires various 3D human characters placed in different virtual 3D scenes. Considering the intra-category variance of “human” category, we leverage the open-source software *MakeHuman* [5] to create diverse 3D human characters with distinct attributes including skeleton, body features (*e.g.*, height, weight, facial components), pose (*e.g.*, walking, running), and clothes. Besides, we leverage the 3D game engine Unity3D and collect different 3D scenes from Unity Asset Store and CG websites, including outdoor scenes (*e.g.*, forest, downtown, street) and indoor scenes (*e.g.*, stadium, gym). Then, we import 3D human characters into the 3D scenes and vary the camera viewpoints to shoot various 2D scenes. Finally, we collect 30 3D scenes and set 50 camera viewpoints for each 3D scene, leading to 1500 2D scenes in total.

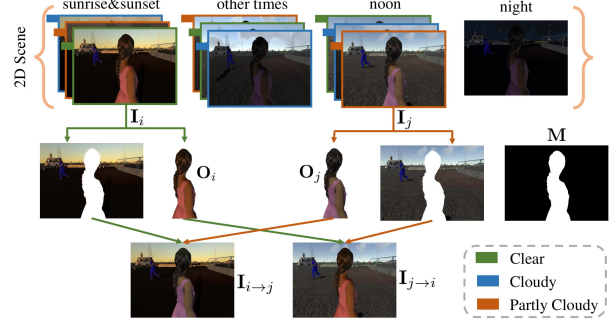


Figure 2: The generation process of composite rendered images. Top row: one 2D scene with 10 different styles. Middle row: exchange the foregrounds between two rendered images with different styles. Bottom row: obtained composite rendered images.

With the assistance of weather system plugin Unisorm, each 2D scene could produce a group of images with different capture conditions (*i.e.*, styles). We select 3 representative weathers (Clear, PartlyCloudy, Cloudy) from Unisorm, and split time-of-the-day into 4 distinct phases (sunrise&sunset, noon, night, other-times). Based on the combinations of weather and time-of-the-day, we define 10 representative styles, including the night style as well as styles of Clear/PartlyCloudy/Cloudy weather at sunrise&sunset/noon/other-times. For each 2D scene, we randomly sample one rendered image from each style, resulting in a group of 10 images. Given 1500 2D scenes, we generate 15,000 rendered images with human foregrounds and different styles. Example rendered images from indoor and outdoor scenes could be found in the Supplementary.

3.2. Composite Rendered Image Generation

As shown in Figure 2, for each 2D scene, we treat one person as foreground and obtain the foreground mask M effortlessly using Unity3D. Assume that we have 10 rendered images $\{I_i\}_{i=1}^{10}$ with different styles $\{y_i\}_{i=1}^{10}$ from the same 2D scene, in which y_i is a 10-dim one-hot style label vector. We denote the foreground person in rendered image I_i as O_i . After randomly selecting two different images I_i and I_j from $\{I_i\}_{i=1}^{10}$, we could generate two pairs of composite rendered images and ground-truth rendered images $\{I_{i \rightarrow j}, I_i\}$ and $\{I_{j \rightarrow i}, I_j\}$ by exchanging O_i and O_j , where $I_{j \rightarrow i}$ denotes the composite rendered image with foreground O_i and background of I_j .

For rendered image pairs $\{I_{j \rightarrow i}, I_j\}$, the style label of ground-truth rendered image I_j is y_j as mentioned above. For composite rendered image $I_{j \rightarrow i}$, we simply assume that its style label vector is weighted average of foreground style y_i and background style y_j : $y_{j \rightarrow i} = r \cdot y_i + (1 - r) \cdot y_j$, in which foreground ratio r denotes the area of foreground over the area of whole image.

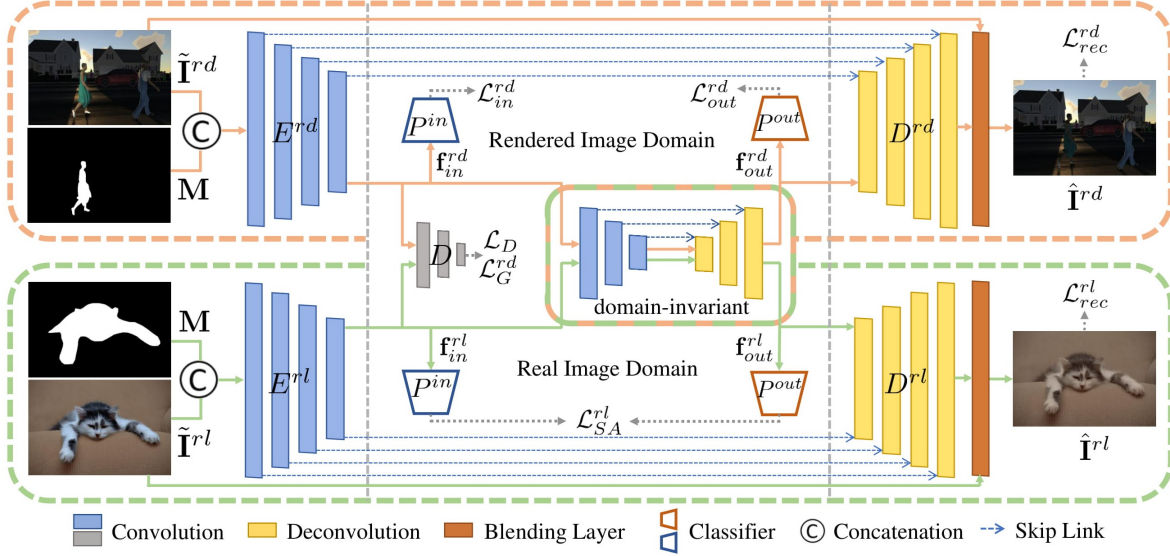


Figure 3: The network architecture of CharmNet, which contains two three-stage generators, a domain discriminator D , and two style classifiers P^{in} and P^{out} . The data flow of real (*resp.*, rendered) images is marked with green (*resp.*, orange) lines.

3.3. Summary of Our Dataset RHHarmony

We have obtained a large-scale rendered image harmonization dataset RHHarmony containing 15,000 ground-truth rendered images, which could maximally generate 135,000 pairs of composite rendered images and ground-truth rendered images. To reduce data redundancy and improve training efficiency, we only use 65,000 pairs to train the harmonization network.

It is worth mentioning that each above-mentioned step (*i.e.*, creating 3D characters, capturing 2D scenes, varying capture conditions, and generating composite rendered images) could be done automatically using scripts, making the dataset efficiently constructed and easily extendable. Besides, with controllable capture conditions (*i.e.*, styles) in Unistorm, it is feasible to acquire ground-truth style labels, which is useful for cross-domain knowledge transfer (see Section 4.2). We will release the RHHarmony dataset and the scripts for automatic construction. Furthermore, we will extend our dataset to cover more categories in the future.

4. Our Method

In this work, we focus on training an image harmonization network using a mixture of rendered image pairs and real image pairs. In the training stage, we have access to rendered (rd) image pairs $\{\tilde{\mathbf{I}}^{rd}, \mathbf{I}^{rd}\}$ from novel categories and real (rl) image pairs $\{\tilde{\mathbf{I}}^{rl}, \mathbf{I}^{rl}\}$ from base categories, where $\tilde{\mathbf{I}}^{rd}$ (*resp.*, $\tilde{\mathbf{I}}^{rl}$) denotes the composite rendered (*resp.*, real) image and \mathbf{I}^{rd} (*resp.*, \mathbf{I}^{rl}) denotes the corresponding ground-truth rendered (*resp.*, real) image. We also have access to the binary foreground mask \mathbf{M} , which is not dis-

tinguished between domains. Given a composite rendered (*resp.*, real) image $\tilde{\mathbf{I}}^{rd}$ (*resp.*, $\tilde{\mathbf{I}}^{rl}$) and mask \mathbf{M} , the goal of image harmonization is to reconstruct \mathbf{I}^{rd} (*resp.*, \mathbf{I}^{rl}) with the harmonized rendered (*resp.*, real) image $\hat{\mathbf{I}}^{rd}$ (*resp.*, $\hat{\mathbf{I}}^{rl}$), whose foreground is expected to be close to that of \mathbf{I}^{rd} (*resp.*, \mathbf{I}^{rl}). In the testing stage, we aim to harmonize composite real images from both base and novel categories.

4.1. Cross-domain Harmonization Network

As mentioned in Section 2.2, after harmonization, the composite rendered (*resp.*, real) image is converted to harmonized rendered (*resp.*, real) image. They share neither the input space nor the output space, so we design a three-stage network for cross-domain harmonization, including a domain-specific encoding stage, a domain-invariant encoding-decoding stage, and a domain-specific decoding stage.

The pipeline of our network is shown in Figure 3. The generator G adopts the improved backbone proposed in iDIH [30], where the image blending layer is added to the UNet-like architecture. Since both input space and output space are different across two domains, we split the first (*resp.*, last) 4 layers in the encoder (*resp.*, decoder) into E^{rd} (*resp.*, D^{rd}) and E^{rl} (*resp.*, D^{rl}), where E^{rd} (*resp.*, E^{rl}) and D^{rd} (*resp.*, D^{rl}) are the domain-specific encoder and decoder for the rendered (*resp.*, real) image domain.

After the domain-specific encoding stage, we assume that images from different domains are projected into the same feature space. Inspired by [10, 11], we employ a domain discriminator D with adversarial loss [38] to further

align two domains, which is given by

$$\begin{aligned}\mathcal{L}_D &= \mathbb{E}[\max(0, 1 - D(\mathbf{f}_{in}^{rl}))] + \mathbb{E}[\max(0, 1 + D(\mathbf{f}_{in}^{rd}))], \\ \mathcal{L}_G^d &= -\mathbb{E}[D(\mathbf{f}_{in}^{rd})],\end{aligned}\quad (1)$$

where \mathbf{f}_{in}^{rd} (*resp.*, \mathbf{f}_{in}^{rl}) denotes the feature extracted by the domain-specific decoder E^{rd} (*resp.*, E^{rl}) in the rendered (*resp.*, real) image domain. By playing a minimax game, the discriminator D encourages the encoders E^{rd} and E^{rl} to project rendered and real images to the same feature space.

Then, through the domain-invariant encoder-decoder, the knowledge of harmonization is transferred from rendered image domain to real image domain. Finally, the third stage projects the domain-invariant features back to the input domain, by enforcing the harmonized output to approach the ground-truth image in each domain:

$$\mathcal{L}_{rec}^{rd} = \|\hat{\mathbf{I}}^{rd} - \mathbf{I}^{rd}\|_1, \quad \mathcal{L}_{rec}^{rl} = \|\hat{\mathbf{I}}^{rl} - \mathbf{I}^{rl}\|_1. \quad (2)$$

4.2. Style Classifiers and Style Aggregation Loss

When a composite rendered image passes through our three-stage network, we assume that the input feature before the second stage is inharmonious with mixed styles as the input composite image, while the output feature after the second stage is harmonious with a unified style as the target ground-truth image. With this assumption, the main harmonization process is accomplished in the second stage, so that more useful knowledge can be transferred from rendered images to real images. Therefore, we employ two auxiliary style classifiers positioned before and after the second stage.

Because rendered images are associated with ground-truth style labels as described in Section 3.2, we adopt standard cross-entropy classification losses for the inharmonious input feature \mathbf{f}_{in}^{rd} and harmonious output feature \mathbf{f}_{out}^{rd} , which is given by

$$\mathcal{L}_{in}^{rd} = -\sum_{k=1}^K \tilde{y}_k^{rd} \log P_k^{in}(\mathbf{f}_{in}^{rd}), \quad (3)$$

$$\mathcal{L}_{out}^{rd} = -\sum_{k=1}^K y_k^{rd} \log P_k^{out}(\mathbf{f}_{out}^{rd}), \quad (4)$$

where K is the number of styles ($K = 10$ as mentioned in Section 3.1). \tilde{y}_k^{rd} (*resp.*, y_k^{rd}) is the k -th entry of style label vector for the composite (*resp.*, ground-truth) rendered image $\hat{\mathbf{I}}^{rd}$ (*resp.*, \mathbf{I}^{rd}). P_k^{in} (*resp.*, P_k^{out}) is the style classifier before (*resp.*, after) the second stage. $P_k^{in}(\cdot)$ or $P_k^{out}(\cdot)$ is the k -th entry of predicted style distribution.

For real images, there exist no ground-truth style labels, so standard classification loss cannot be used. Since the foreground style should be harmonized to the same as background style during harmonization, we design a novel style aggregation (SA) loss composed of two loss terms based on the following two assumptions. Firstly, \mathbf{f}_{out}^{rl} is likely to have

one style only if \mathbf{f}_{in}^{rl} has this style. So we adopt the weighted classification loss:

$$\mathcal{L}_W^{rl} = -\sum_{k=1}^K P_k^{in}(\mathbf{f}_{in}^{rl}) \log P_k^{out}(\mathbf{f}_{out}^{rl}). \quad (5)$$

Intuitively, if $P_k^{in}(\mathbf{f}_{in}^{rl})$ is small, $P_k^{out}(\mathbf{f}_{out}^{rl})$ would also be penalized. Because rendered images and real images are projected to the same feature space after the first stage, P^{in} and P^{out} are shared across two domains.

Secondly, the style distribution of \mathbf{f}_{out}^{rl} should be more concentrated than that of \mathbf{f}_{in}^{rl} . Since entropy depends on concentration and lower entropy implies higher concentration, we propose an entropy reduction loss to guarantee that the style distribution becomes more concentrated after harmonization:

$$\begin{aligned}\mathcal{L}_{ER}^{rl} &= \max(0, m) + \sum_{k=1}^K P_k^{in}(\mathbf{f}_{in}^{rl}) \log P_k^{in}(\mathbf{f}_{in}^{rl}) \\ &\quad - \sum_{k=1}^K P_k^{out}(\mathbf{f}_{out}^{rl}) \log P_k^{out}(\mathbf{f}_{out}^{rl}),\end{aligned}\quad (6)$$

where m is a margin. We wrap up the above two loss terms as a style aggregation loss $\mathcal{L}_{SA}^{rl} = \mathcal{L}_W^{rl} + \mathcal{L}_{ER}^{rl}$. Then, the total loss function for training the generators is

$$\begin{aligned}\mathcal{L}_G &= \mathcal{L}_{rec}^{rd} + \mathcal{L}_{rec}^{rl} + \lambda_{adv} \mathcal{L}_G^{rd} \\ &\quad + \lambda_{sty}^{rd} (\mathcal{L}_{in}^{rd} + \mathcal{L}_{out}^{rd}) + \lambda_{sty}^{rl} \mathcal{L}_{SA}^{rl},\end{aligned}\quad (7)$$

where λ_{adv} , λ_{sty}^{rd} , and λ_{sty}^{rl} are trade-off parameters.

5. Experiments

5.1. Dataset Statistics

Rendered Image Dataset RHHarmony contains 65,000 pairs of composite rendered images and ground-truth rendered images with human foregrounds for training.

Real Image Dataset iHarmony4 [6] contains 73,146 pairs of composite real images and ground-truth real images. In this work, we treat “human” as novel category and other categories as base categories. The training set is split into novel training set (18,718 pairs) from “human” category and base training set (47,024 pairs) from other categories. Similarly, the test set is split into novel test set (1670 pairs) and base test set (5734 pairs).

Formally, we denote the rendered training set from novel category as $\mathcal{D}_{tr,n}^{rd}$ and the real training set from base (*resp.*, novel) categories as $\mathcal{D}_{tr,b}^{rl}$ (*resp.*, $\mathcal{D}_{tr,n}^{rl}$). We denote real test set from base (*resp.*, novel) categories as $\mathcal{D}_{te,b}^{rl}$ (*resp.*, $\mathcal{D}_{te,n}^{rl}$). By default, we merge $\mathcal{D}_{tr,n}^{rd}$ and $\mathcal{D}_{tr,b}^{rl}$ as the whole training set, and evaluate on both $\mathcal{D}_{te,b}^{rl}$ and $\mathcal{D}_{te,n}^{rl}$ (see Figure 1).

#	Training data	Method	$\mathcal{D}_{te,n}^{rl}$			$\mathcal{D}_{te,b}^{rl}$		
			MSE↓	fMSE↓	PSNR↑	MSE↓	fMSE↓	PSNR↑
1	-	Input Composite	155.74	931.74	33.29	177.34	1505.92	31.15
2	$\mathcal{D}_{tr,b}^{rl}$	DoveNet [6]	69.06	458.15	35.01	65.87	674.57	33.94
3		Hao <i>et al.</i> [16]	52.42	407.26	35.43	58.21	582.79	34.54
4		iDIH [30]	46.67	417.71	35.21	53.03	566.96	34.77
5	$\mathcal{D}_{tr,n}^{rd} \& \mathcal{D}_{tr,b}^{rl}$	two-stage training	43.06	383.39	35.67	49.56	533.10	34.98
6		dataset fusion	38.31	368.50	35.64	44.15	485.94	35.27
7		UNIT [25]	55.09	458.72	34.74	56.21	607.14	34.38
8		CycleGAN [45]	51.82	474.78	34.64	56.30	592.33	34.52
9		CharmNet	30.83	296.40	36.60	39.41	432.19	35.83
10	$\mathcal{D}_{tr,n}^{rl} \& \mathcal{D}_{tr,b}^{rl}$	iDIH [30]	27.71	259.17	37.12	36.17	422.98	36.04

Table 1: Results of models trained on various training data and tested on $\mathcal{D}_{te,n}^{rl}/\mathcal{D}_{te,b}^{rl}$. “-” denotes metrics directly tested on composite real images. Note that row 10 using real training images $\mathcal{D}_{tr,n}^{rl}$ from novel category serves as the upper bound.

#	Training data	fMSE↓	PSNR↑
1	-	931.74	33.29
2	$\mathcal{D}_{tr,n}^{rl}$	386.36	35.71
3	$\mathcal{D}_{tr,b}^{rl}(sub)$	486.54	34.64
4	$\mathcal{D}_{tr,n}^{rd}(sub)$	1100.86	31.25

Table 2: The results of models that are trained on $\mathcal{D}_{tr,n}^{rl}$, $\mathcal{D}_{tr,b}^{rl}(sub)$, and $\mathcal{D}_{tr,n}^{rd}(sub)$ and tested on $\mathcal{D}_{te,n}^{rl}$. “-” denotes the metrics directly tested on the composite real images.

5.2. Implementation Details

We adopt the UNet-like architecture of iDIH [30] as backbone considering its simplicity and effectiveness. Note that we do not use auxiliary semantic information as in [30] for brevity and fair comparison with other methods. As in Figure 3, the domain-specific encoder (*resp.*, decoder) contains the first (*resp.*, last) 4 layers in the encoder (*resp.*, decoder). And the other layers form the domain-invariant encoder-decoder. In our experiments, λ_{adv} , λ_{sty}^{rd} , and λ_{sty}^{rl} are set to 0.1, 0.1, and 0.05, respectively. Following [6], we use MSE, fMSE (foreground MSE), and PSNR calculated on 256×256 images as the main evaluation metrics. More details could be found in the Supplementary.

5.3. Preliminary Results

First, we evaluate the performance of cross-category harmonization. We train iDIH [30] on $\mathcal{D}_{tr,n}^{rl}$ and test on $\mathcal{D}_{te,n}^{rl}$. Then, we switch the training set to $\mathcal{D}_{tr,b}^{rl}$. The size of $\mathcal{D}_{tr,n}^{rl}$ is $N = 18718$. For fair comparison, we sample the equal number N of real training images from $\mathcal{D}_{tr,b}^{rl}$, forming the sub training set $\mathcal{D}_{tr,b}^{rl}(sub)$. By comparing row 2 and row 3 in Table 2, we observe that although cross-category harmonization could harmonize the composite images (row 1 *v.s.* row 3), its performance is much worse than within-category

harmonization (row 2 *v.s.* row 3).

Next, we evaluate the performance of cross-domain harmonization by switching the training set to $\mathcal{D}_{tr,n}^{rd}$. We sample N rendered training images from $\mathcal{D}_{tr,n}^{rd}$, forming the sub training set $\mathcal{D}_{tr,n}^{rd}(sub)$. By comparing row 2 and row 4 in Table 2, cross-domain harmonization hurts the performance badly, which demonstrates the large domain gap between rendered images and real images.

In summary, without real training images from novel category $\mathcal{D}_{tr,n}^{rl}$, solely using $\mathcal{D}_{tr,b}^{rl}$ or using $\mathcal{D}_{tr,n}^{rd}$ will both lead to sub-optimal performance, which motivates us to train with a mixture of $\mathcal{D}_{tr,b}^{rl}$ and $\mathcal{D}_{tr,n}^{rd}$.

5.4. Main Results

As shown in Table 1, we divide baselines into two groups according to their used training data. The first group contains three recent image harmonization baselines (row 2 to row 4) that are trained with only $\mathcal{D}_{tr,b}^{rl}$. Among them, iDIH [30] achieves competitive performance, so the rest baselines (row 5 to row 8) and our method are all built upon iDIH. The second group contains domain adaptation models trained with both $\mathcal{D}_{tr,n}^{rd}$ and $\mathcal{D}_{tr,b}^{rl}$. Since there are no existing domain adaptation methods that could be directly applied to our task, we evaluate two straightforward methods, *i.e.*, two-stage training and dataset fusion, as well as Image-to-Image (I2I) translation methods [25, 45] for comparison. Specifically, two-stage training means training with $\mathcal{D}_{tr,n}^{rd}$ and fine-tuning with $\mathcal{D}_{tr,b}^{rl}$. Dataset fusion means directly training with a combination of $\mathcal{D}_{tr,n}^{rd}$ and $\mathcal{D}_{tr,b}^{rl}$. For I2I translation methods, we train UNIT [25] and CycleGAN [45] to translate from rendered image domain $\mathcal{D}_{tr,n}^{rd}$ to real image domain $\mathcal{D}_{tr,b}^{rl}$. Then, we use translated $\mathcal{D}_{tr,n}^{rd}$ to augment $\mathcal{D}_{tr,b}^{rl}$ as the new training set.

The results of the second baseline group are also reported in Table 1. Two-stage training only brings minor perfor-

\mathcal{L}_G^{rd}	\mathcal{L}_{in}^{rd}	\mathcal{L}_{out}^{rd}	\mathcal{L}_W^{rl}	\mathcal{L}_{ER}^{rl}	fMSE ↓	PSNR ↑
					339.02	36.06
✓					303.69	36.45
✓	✓	✓			300.22	36.50
✓	✓	✓	✓		297.99	36.52
✓	✓	✓		✓	297.94	36.51
✓	✓	✓	✓	✓	296.40	36.60

Table 3: Ablation studies on the losses. The results are tested on $\mathcal{D}_{te,n}^{rl}$.

mance gain (row 5 v.s. row 4), probably because the statistics of real image domain are only considered during the second stage. The dataset fusion method improves the performance by a large margin (row 6 v.s. row 4), which indicates that RHHarmony, though a rendered image dataset, is complementary to real image dataset by providing essential information of novel category. Another observation is that the performances of UNIT and CycleGAN are significantly degraded and even worse than iDIH (row 4). The reason is that the quality of translated images is very low and the illumination statistics are severely distorted. Our proposed CharmNet outperforms all the baselines within the second group by a large margin. Apart from novel category, our method also significantly enhances the performance on base categories, which indicates that cross-domain cross-category knowledge transfer is also very useful.

In addition, we report the result of iDIH trained with both $\mathcal{D}_{tr,n}^{rl}$ and $\mathcal{D}_{tr,b}^{rl}$ (row 10). This model serves as an upper bound for domain adaptation methods, assuming that there are abundant real training images from novel category. Despite the performance gap between row 9 and row 10, our method has shown great potential to bridge the gap between real images and rendered images. Since extending rendered image dataset costs significantly fewer manual efforts than extending real image dataset, we firmly believe that using both rendered images and real images for image harmonization is a promising research direction.

5.5. Ablation Studies

Loss Design: First, we ablate each component of the loss function in Table 3. When we use neither adversarial loss nor style-related losses, the network only contains two three-stage generators. Though the performance is degraded, it is still better than iDIH (row 4 in Table 1) due to the information sharing in the second stage. By adding adversarial loss \mathcal{L}_G^{rd} after the first stage, the performance is boosted, which demonstrates the efficacy of adversarial loss to pull close two domains. Besides, after adding two style losses \mathcal{L}_{in}^{rd} and \mathcal{L}_{out}^{rd} in the rendered image domain, the performance is further improved, which indicates the potential of available style information. We ablate the style

L of E^r	L of D^r	fMSE ↓	PSNR ↑
0	7	498.82	34.48
3	3	327.45	36.20
4	4	296.40	36.60
5	5	328.39	36.19
7	0	501.67	34.58

Table 4: Ablation studies on the hyper-parameter L . We use E^r (resp., D^r) to represent both E^{rd} (resp., D^{rd}) and E^{rl} (resp., D^{rl}). “ L of E^r (resp., D^r)” denotes the number of unshared layers in the first (resp., third) stage. The results are tested on $\mathcal{D}_{te,n}^{rl}$.

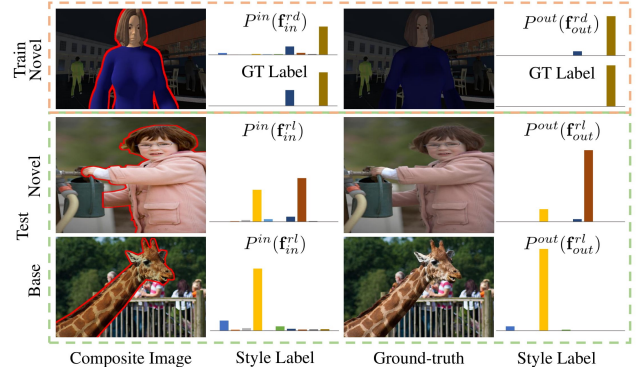


Figure 4: The style distribution analyses for the rendered training image from novel category and the real test images from base and novel categories.

aggregation loss \mathcal{L}_{SA}^{rl} by its two terms \mathcal{L}_W^{rl} and \mathcal{L}_{ER}^{rl} . The results demonstrate that each term is helpful and their combination achieves further improvement with mutual collaboration. Besides, we show the harmonization results under different loss designs in Supplementary.

Network Design: As mentioned in Section 4.1, we empirically split the first (resp., last) L layers in encoder (resp., decoder) into the first (resp., third) stage. Therefore, we also investigate the impact of hyper-parameter L , and the results are reported in Table 4. When we increase L to 5, the performance is degraded, since it hampers the useful information sharing in the second stage. In addition, when we decrease L to 3, the performance is also degraded, possibly because it brings difficulty in aligning the extracted features from two domains.

We also explore the extreme cases where all the encoder or decoder layers are shared across domains. Setting L of E^r (resp., D^r) to 0 means sharing the entire encoder (resp., decoder). The performances in both cases are significantly dropped. This is because the input space and output space for image harmonization are the same in each domain but different across domains. Simply sharing the entire encoder or decoder will hurt the cross-domain transfer.



Figure 5: Example results generated by different baselines and our method on $\mathcal{D}_{te,n}^{rl}$. From left to right, we show the input composite real image, ground-truth real image, as well as the harmonized images generated by iDIH [30] backbone, CycleGAN [45], dataset fusion, and our CharmNet. The foregrounds are highlighted with red border lines.

Hyper-parameter Analyses: We also investigate the impact of the other four hyper-parameters in the loss functions, including margin m in Eqn. 6, trade-off parameters λ_{adv} , λ_{sty}^d , and λ_{sty}^{rl} in Eqn. 7. Due to space limitation, we leave the detailed experimental results to Supplementary.

5.6. Training Data Analyses

We explore the performance variance when using different numbers of rendered training images. We also explore the performance variance of the whole $\mathcal{D}_{tr,n}^{rd}$ when there are inadequate numbers of real training images from novel category. The detailed results are also left to Supplementary.

5.7. Style Distribution Analyses

Recall that in Section 4.2, we leverage the ground-truth style labels in the rendered image domain and design a style aggregation loss in the real image domain to facilitate cross-domain knowledge transfer. To verify that the knowledge transfer is well-behaved, we conduct style distribution analyses on both domains. As shown in Figure 4, in rendered image domain, with classification losses, the style prediction of \mathbf{f}_{in}^{rd} (resp., \mathbf{f}_{out}^{rd}) is close to the ground-truth style label of the composite (resp., ground-truth) rendered image. In the real image domain, we select two real test examples from $\mathcal{D}_{te,b}^{rl}$ and $\mathcal{D}_{te,n}^{rl}$ respectively. With style aggregation loss, the style prediction of \mathbf{f}_{out}^{rl} is more concentrated than that of \mathbf{f}_{in}^{rl} in both cases. For example, in the second

row, $P^{in}(\mathbf{f}_{in}^{rl})$ includes a primary style of cloudy weather at other times and a secondary style of clear weather at noon. After harmonization, $P^{out}(\mathbf{f}_{out}^{rl})$ only has one dominant style (i.e., cloudy weather at other times), demonstrating that style knowledge is well-transferred across domains.

5.8. Qualitative Analyses

Given a composite real image from $\mathcal{D}_{te,n}^{rl}$, the harmonized outputs generated by iDIH [30] (row 4 in Table 1), CycleGAN [45], dataset fusion, and our CharmNet are shown in Figure 5. Compared with other baselines, CharmNet could generate more favorable results with consistent foreground and background. Besides, CharmNet concentrates more on adjusting the foreground style to the background style without corrupting the appearance of human foreground, making the harmonized results visually closer to the ground-truth real images. Besides, in the Supplementary, we provide example results on $\mathcal{D}_{te,b}^{rl}$ and compare the harmonization results of our method and upper bound (row 10 in Table 1).

In real-world applications, there is no ground-truth for a real-world composite image with human foreground, so it is infeasible to evaluate the model performance quantitatively using MSE or PSNR. Following [6, 7, 37], we select 46 images with human foregrounds from the real-world composite images released in [37] and conduct user study. The detailed user study and harmonization results can also be

found in the Supplementary.

6. Conclusion

In this paper, we have contributed a large-scale rendered human harmonization dataset RHHarmony. We have also presented a cross-domain image harmonization network. Our constructed dataset and proposed network have made a big step towards bridging the gap between rendered images and real images for image harmonization.

References

- [1] Rita Chattopadhyay, Qian Sun, Wei Fan, Ian Davidson, Sethuraman Panchanathan, and Jieping Ye. Multisource domain adaptation and its application to early detection of fatigue. *ACM Trans. Knowl. Discov. Data*, 6(4), 2012. 3
- [2] Yuhua Chen, Wen Li, Christos Sakaridis, Dengxin Dai, and Luc Van Gool. Domain adaptive faster r-cnn for object detection in the wild. In *CVPR*, 2018. 3
- [3] Yunjey Choi, Min-Je Choi, Munyoung Kim, Jung-Woo Ha, Sunghun Kim, and Jaegul Choo. StarGAN: Unified generative adversarial networks for multi-domain image-to-image translation. In *CVPR*, 2018. 3
- [4] Daniel Cohen-Or, Olga Sorkine, Ran Gal, Tommer Leyvand, and Ying-Qing Xu. Color harmonization. *ACM Transactions on Graphics*, 25(3):624–630, 2006. 2
- [5] MakeHuman Community. MakeHuman: Open source tool for making 3D characters. <http://www.makehumancommunity.org>. 3
- [6] Wenyan Cong, Jianfu Zhang, Li Niu, Liu Liu, Zhixin Ling, Weiyan Li, and Liqing Zhang. DoveNet: Deep image harmonization via domain verification. In *CVPR*, 2020. 1, 2, 5, 6, 8
- [7] Xiaodong Cun and Chi-Man Pun. Improving the harmony of the composite image by spatial-separated attention module. *IEEE Trans. Image Process.*, 29:4759–4771, 2020. 1, 2, 8
- [8] W. Deng, L. Zheng, Q. Ye, G. Kang, Y. Yang, and J. Jiao. Image-image domain adaptation with preserved self-similarity and domain-dissimilarity for person re-identification. In *CVPR*, 2018. 3
- [9] Yang Fu, Yunchao Wei, Guanshuo Wang, Yuqian Zhou, Honghui Shi, and Thomas S. Huang. Self-similarity grouping: A simple unsupervised cross domain adaptation approach for person re-identification. In *ICCV*, 2019. 3
- [10] Yaroslav Ganin and Victor Lempitsky. Unsupervised domain adaptation by backpropagation. In *ICML*, 2015. 4
- [11] Yaroslav Ganin, Evgeniya Ustinova, Hana Ajakan, Pascal Germain, Hugo Larochelle, François Laviolette, Mario Marchand, and Victor Lempitsky. Domain-adversarial training of neural networks. *J. Mach. Learn. Res.*, 17(1):2096–2030, 2016. 4
- [12] W. Ge, S. Yang, and Y. Yu. Multi-evidence filtering and fusion for multi-label classification, object detection and semantic segmentation based on weakly supervised learning. In *CVPR*, 2018. 3
- [13] T. Gebru, J. Hoffman, and L. Fei-Fei. Fine-grained recognition in the wild: A multi-task domain adaptation approach. In *ICCV*, 2017.
- [14] Xavier Glorot, Antoine Bordes, and Yoshua Bengio. Domain adaptation for large-scale sentiment classification: A deep learning approach. In *ICML*, 2011.
- [15] R. Gopalan, Ruonan Li, and R. Chellappa. Domain adaptation for object recognition: An unsupervised approach. In *ICCV*, 2011. 3
- [16] Guoqing Hao, Satoshi Iizuka, and Kazuhiro Fukui. Image harmonization with attention-based deep feature modulation. In *BMVC*, 2020. 1, 2, 6
- [17] Xun Huang, Ming-Yu Liu, Serge J. Belongie, and Jan Kautz. Multimodal unsupervised image-to-image translation. In *ECCV*, 2018. 3
- [18] N. Inoue, R. Furuta, T. Yamasaki, and K. Aizawa. Cross-domain weakly-supervised object detection through progressive domain adaptation. In *CVPR*, 2018. 3
- [19] Phillip Isola, Jun-Yan Zhu, Tinghui Zhou, and Alexei A. Efros. Image-to-image translation with conditional adversarial networks. In *CVPR*, 2017. 3
- [20] Jiaya Jia, Jian Sun, Chi-Keung Tang, and Heung-Yeung Shum. Drag-and-drop pasting. *ACM Transactions on Graphics*, 25(3):631–637, 2006. 2
- [21] Seunghyeon Kim, Jaehoon Choi, Taekyung Kim, and Chang-ick Kim. Self-training and adversarial background regularization for unsupervised domain adaptive one-stage object detection. In *ICCV*, 2019. 3
- [22] Jean-François Lalonde and Alexei A. Efros. Using color compatibility for assessing image realism. In *ICCV*, 2007. 2
- [23] Hsin-Ying Lee, Hung-Yu Tseng, Jia-Bin Huang, Maneesh Singh, and Ming-Hsuan Yang. Diverse image-to-image translation via disentangled representations. In *ECCV*, 2018. 3
- [24] Hsin-Ying Lee, Hung-Yu Tseng, Qi Mao, Jia-Bin Huang, Yu-Ding Lu, Maneesh Singh, and Ming-Hsuan Yang. Drit++: Diverse image-to-image translation via disentangled representations. *International Journal of Computer Vision*, pages 1–16, 2020.
- [25] Ming-Yu Liu, Thomas Breuel, and Jan Kautz. Unsupervised image-to-image translation networks. In *NeurIPS*, volume 30, 2017. 6
- [26] Ming-Yu Liu, Xun Huang, Arun Mallya, Tero Karras, Timo Aila, Jaakko Lehtinen, and Jan Kautz. Few-shot unsupervised image-to-image translation. In *ICCV*, 2019. 3
- [27] Patrick Pérez, Michel Gangnet, and Andrew Blake. Poisson image editing. *ACM Transactions on Graphics*, 22(3):313–318, 2003. 2
- [28] François Pitie, Anil C Kokaram, and Rozenn Dahyot. N-dimensional probability density function transfer and its application to color transfer. In *ICCV*, pages 1434–1439, 2005. 2
- [29] Erik Reinhard, Michael Ashikhmin, Bruce Gooch, and Peter Shirley. Color transfer between images. *IEEE Computer Graphics and Applications*, 21(5):34–41, 2001. 2
- [30] Konstantin Sofiiuk, Polina Popenova, and Anton Konushin. Foreground-aware semantic representations for image harmonization. In *WACV*, 2021. 1, 2, 4, 6, 8
- [31] A. Spurr, J. Song, S. Park, and O. Hilliges. Cross-modal deep variational hand pose estimation. In *CVPR*, 2018. 3
- [32] Kalyan Sunkavalli, Micah K. Johnson, Wojciech Matusik, and Hanspeter Pfister. Multi-scale image harmonization.

ACM Transactions on Graphics, 29(4):125:1–125:10, 2010.

2

- [33] Fuwen Tan, Crispin Bernier, Benjamin Cohen, Vicente Ordonez, and Connelly Barnes. Where and who? automatic semantic-aware person composition. In *WACV*, 2018. 2
- [34] Michael W. Tao, Micah K. Johnson, and Sylvain Paris. Error-tolerant image compositing. In *ECCV*, 2010. 2
- [35] Unity Technologies. Unity3D: Cross-platform game engine. <https://unity.com>. 2
- [36] Antonio Torralba and Alexei A Efros. Unbiased look at dataset bias. In *CVPR*, 2011. 2
- [37] Yi-Hsuan Tsai, Xiaohui Shen, Zhe Lin, Kalyan Sunkavalli, Xin Lu, and Ming-Hsuan Yang. Deep image harmonization. In *CVPR*, 2017. 1, 2, 8
- [38] E. Tzeng, J. Hoffman, K. Saenko, and T. Darrell. Adversarial discriminative domain adaptation. In *CVPR*, 2017. 4
- [39] Tuan-Hung Vu, Himalaya Jain, Maxime Bucher, Matthieu Cord, and Patrick Perez. ADVENT: Adversarial entropy minimization for domain adaptation in semantic segmentation. In *CVPR*, 2019. 3
- [40] L. Wei, S. Zhang, W. Gao, and Q. Tian. Person transfer gan to bridge domain gap for person re-identification. In *CVPR*, 2018. 3
- [41] Shuchen Weng, Wenbo Li, Dawei Li, Hongxia Jin, and Boxin Shi. MISC: Multi-condition injection and spatially-adaptive compositing for conditional person image synthesis. In *CVPR*, 2020. 2
- [42] Su Xue, Aseem Agarwala, Julie Dorsey, and Holly E. Rushmeier. Understanding and improving the realism of image composites. *ACM Transactions on Graphics*, 31(4):84:1–84:10, 2012. 2
- [43] Y. Zhang, P. David, and B. Gong. Curriculum domain adaptation for semantic segmentation of urban scenes. In *ICCV*, 2017. 2, 3
- [44] Xingyi Zhou, Arjun Karpur, Chuang Gan, Linjie Luo, and Qixing Huang. Unsupervised domain adaptation for 3d key-point estimation via view consistency. In *ECCV*, 2018. 3
- [45] Jun-Yan Zhu, Taesung Park, Phillip Isola, and Alexei A. Efros. Unpaired image-to-image translation using cycle-consistent adversarial networks. In *ICCV*, 2017. 3, 6, 8
- [46] Yang Zou, Zhiding Yu, B. V. Kumar, and J. Wang. Unsupervised domain adaptation for semantic segmentation via class-balanced self-training. In *ECCV*, 2018. 3

Supplementary Material for Deep Image Harmonization by Bridging the Reality Gap

In the Supplementary file, we will first show example ground-truth rendered images of our contributed dataset RHHarmony in Section S1, and introduce the implementation details in Section S2. Then, we will show example results under different loss designs and analyze the impact of different hyper-parameters in Section S3. We will explore the performance variance using different settings of training data in Section S4. Besides, we will exhibit the harmonization results of different methods on real test set $\mathcal{D}_{te,b}^{rl}$ from base categories in Section S5 and compare our method with the upper bound (row 10 in Table 1 in the main paper) in Section S6. Finally, we will introduce more details of user study conducted on 46 real-world composite images with human foregrounds and show example harmonization results of different methods in Section S7.

S1. Example Ground-truth Rendered Images of Our RHHarmony Dataset

As mentioned in Section 3.1 in the main text, we collect 30 3D scenes from Unity Asset Store and CG websites, including outdoor scenes (*e.g.*, raceway, downtown, street, forest) and indoor scenes (*e.g.*, bar, stadium, gym). For each 2D scene shot in 3D scenes, we sample 10 ground-truth rendered images with 10 different capture conditions (*i.e.*, styles), including the the night style as well as styles of Clear/PartlyCloudy/Cloudy weather at sunrise&sunset/noon/other-times. In Figure S1, we select some indoor/outdoor 2D scenes, and exhibit all 10 ground-truth rendered images for each 2D scene, which provides an intuitive perspective for the diversity of our contributed rendered image dataset RHHarmony.

S2. Implementation Details

Our network is implemented using Pytorch 1.4.0 and trained on ubuntu 16.04 LTS operation system, with 64GB memory, Intel Core i7-8700K CPU, and two GeForce GTX 1080 Ti GPUs.

The discriminator D consists of 3 convolution layers with channel number $\{64, 32, 1\}$, 3×3 kernels and stride of 1, each of which is followed by a Leaky-ReLU except the last one. The style classifiers P^{in} and P^{out} are the same in the structure and shared across domains. They contain 4 convolution layers with channel number $\{64, 32, 16, 1\}$, 3×3 kernels and stride of 1, each of which is followed by a BatchNorm, a ReLU, and a max-pooling layer except the last one.

To train the network, we use Adam optimizer with $\beta_1 = 0.9$ and $\beta_2 = 0.999$. Learning rate is initialized with $1e^{-4}$ and reduced by a factor of 10 at epochs 100 and 120.

S3. Ablation Studies

S3.1. Results under Different Loss Designs

In Section 5.5 in the main text, we ablate each component of the loss functions, including \mathcal{L}_G^{rd} , \mathcal{L}_{in}^{rd} , \mathcal{L}_{out}^{rd} , \mathcal{L}_W^{rl} , and \mathcal{L}_{ER}^{rl} . Recall that \mathcal{L}_W^{rl} and \mathcal{L}_{ER}^{rl} are two terms of the style aggregation loss \mathcal{L}_{SA}^{rl} .

In this section, we present example test images from $\mathcal{D}_{te,n}^{rl}$ harmonized under four different loss designs, including $\mathcal{L}_{rec}^{rd} + \mathcal{L}_{rec}^{rl}$ (row 1 in Table 3 in the main text), $\mathcal{L}_{rec}^{rd} + \mathcal{L}_{rec}^{rl} + \mathcal{L}_G^{rd}$ (row 2), $\mathcal{L}_{rec}^{rd} + \mathcal{L}_{rec}^{rl} + \mathcal{L}_G^{rd} + \mathcal{L}_{in}^{rd} + \mathcal{L}_{out}^{rd}$ (row 3), and our full method $\mathcal{L}_{rec}^{rd} + \mathcal{L}_{rec}^{rl} + \mathcal{L}_G^{rd} + \mathcal{L}_{in}^{rd} + \mathcal{L}_{out}^{rd} + \mathcal{L}_{SA}^{rl}$ (row 6). The results are shown in Figure S2. We observe that our CharmNet could produce more harmonious results that are closer to the ground-truth real images. By comparing the results of “Sim 1” and “Sim 2” in Figure S2, it can be seen that adversarial loss \mathcal{L}_G^{rd} is important for aligning two domains to generate reasonable harmonized results. By comparing the results of “Sim 2”, “Sim 3” and “Full Version”, it can be seen that style classification losses $\mathcal{L}_{in}^{rd} + \mathcal{L}_{out}^{rd}$ in the rendered image domain and the style aggregation loss \mathcal{L}_{SA}^{rl} in the real image domain are both meaningful for image harmonization, and their combination ensures the useful knowledge transfer across domains, thus leading to a more satisfactory performance.

S3.2. Hyper-parameter Analyses

We investigate the impact of four hyper-parameters: the margin m in Eqn. 6 and trade-off parameters λ_{adv} , λ_{sty} , and λ_{sty}^{rl} in Eqn. 7 in the main text. In Figure S3, we plot the performance on $\mathcal{D}_{te,n}^{rl}$ by varying each hyper-parameter while keeping the other hyper-parameters fixed. It can be seen that our method is robust with hyper-parameters in reasonable ranges (*i.e.*, m in range $[2^{-2}, 2^2]$, λ_{adv} and λ_{sty}^{rd} in range $[10^{-3}, 1]$ and λ_{sty}^{rl} in range $[5 \times 10^{-4}, 5 \times 10^{-1}]$).

S4. Training Data Analyses

In the experiments in the main paper, we use 65k rendered training images in $\mathcal{D}_{tr,n}^{rd}$. Here, we explore the performance variance when using different numbers of rendered training images. Specifically, we use the full set of $\mathcal{D}_{tr,b}^{rd}$ and a subset of $\mathcal{D}_{tr,n}^{rd}$ (*i.e.*, $\mathcal{D}_{tr,n}^{rd}(sub)$) with various numbers of rendered training images to train our CharmNet, and evaluate the model on both $\mathcal{D}_{te,n}^{rl}$ and $\mathcal{D}_{te,b}^{rl}$. As shown in Figure S4a and Figure S4b, the performance improves with an increasing size of $\mathcal{D}_{tr,n}^{rd}(sub)$. Though the performance growth slows down when the size approaches 65k, the best performance is still obtained under the full set of $\mathcal{D}_{tr,n}^{rd}$. Note that introducing more rendered training images will bring marginal improvement yet higher computational cost, so we use 65k rendered training images by default.

Besides, we explore another experimental setup, where real training set has inadequate number of examples from novel category. It is very common that the real training set has a few yet insufficient examples for certain categories, in which case we can enrich the real training set with rendered images from these categories. Specifically, we use the full set of $\mathcal{D}_{tr,b}^{rl}$ and a subset of $\mathcal{D}_{tr,n}^{rl}$ (*i.e.*, $\mathcal{D}_{tr,n}^{rl}(sub)$) with various numbers of real training images from novel category to train the iDIH [S5] backbone. In addition, for each size of $\mathcal{D}_{tr,n}^{rl}(sub)$, we also augment the training set with the full set of $\mathcal{D}_{tr,n}^{rd}$ to train our CharmNet. The trained models are evaluated on both $\mathcal{D}_{te,n}^{rl}$ and $\mathcal{D}_{te,b}^{rl}$ for comparison. The results are shown in Figure S4c and Figure S4d, from which we have three observations. Firstly, no matter using rendered images or not, increasing the size of $\mathcal{D}_{tr,n}^{rl}(sub)$ will bring consistent performance improvement. Secondly, with a specific size of $\mathcal{D}_{tr,n}^{rl}(sub)$ (*e.g.*, 5k), using rendered training images $\mathcal{D}_{tr,n}^{rd}$ from novel cat-

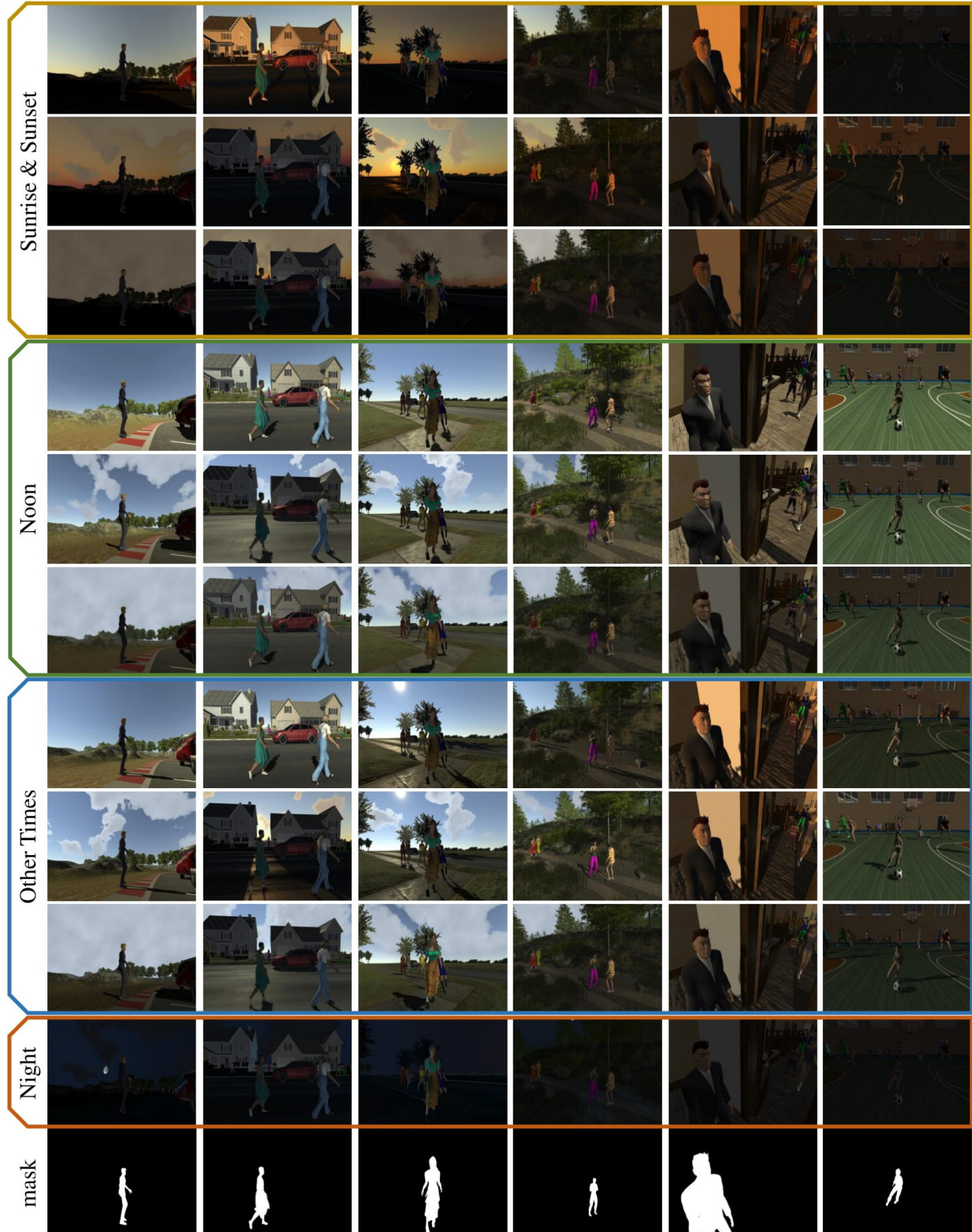


Figure S1: Example ground-truth rendered images in RHHarmony dataset. The left four columns are outdoor scenes (raceway, downtown, street, and forest) and the right two columns are indoor scenes (bar and stadium). Under each time of the day except “Night”, from top to bottom, we show rendered images captured under Clear, Partly Cloudy, and Cloudy weather.

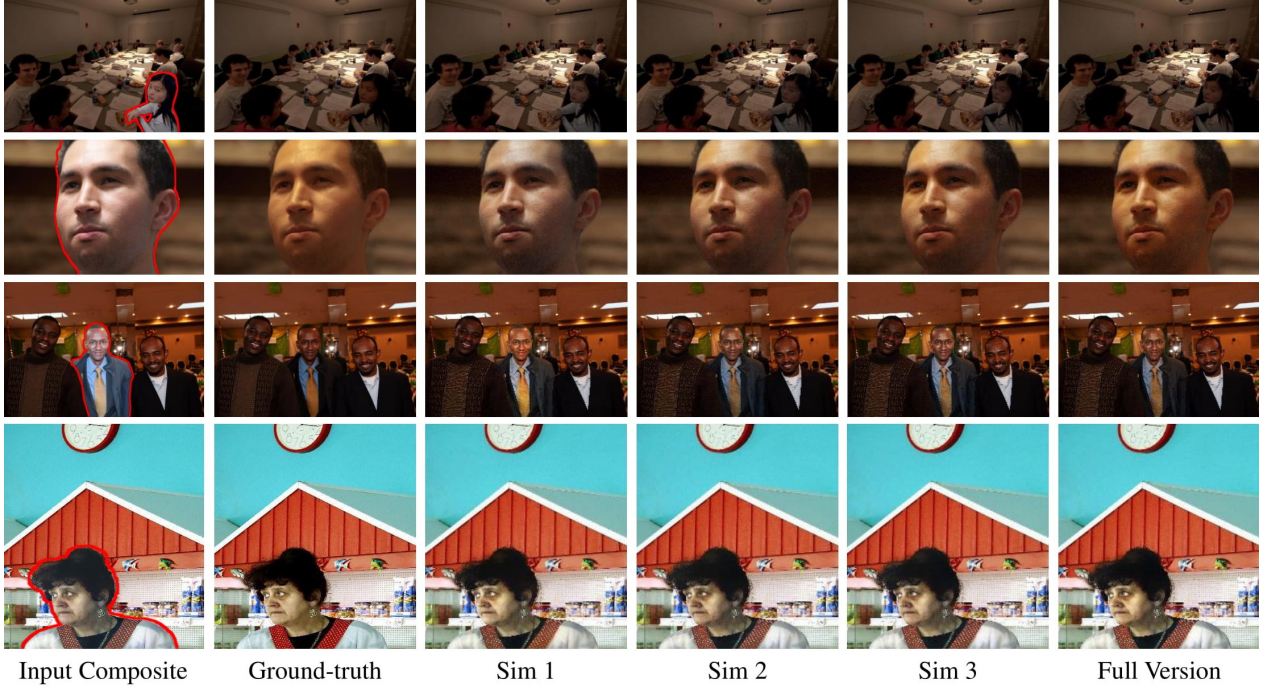


Figure S2: Example results generated under different loss designs on $\mathcal{D}_{te,n}^{rl}$. From left to right, we show the input composite real image, ground-truth real image, as well as the harmonized results generated by Sim 1, Sim 2, Sim 3, and our full method CharmNet, where Sim 1 = $\mathcal{L}_{rec}^{rd} + \mathcal{L}_{rec}^{rl}$, Sim 2 = $\mathcal{L}_{rec}^{rd} + \mathcal{L}_{rec}^{rl} + \mathcal{L}_G^{rd}$, Sim 3 = $\mathcal{L}_{rec}^{rd} + \mathcal{L}_{rec}^{rl} + \mathcal{L}_G^{rd} + \mathcal{L}_{in}^{rd} + \mathcal{L}_{out}^{rd}$, and Full Version = $\mathcal{L}_{rec}^{rd} + \mathcal{L}_{rec}^{rl} + \mathcal{L}_G^{rd} + \mathcal{L}_{in}^{rd} + \mathcal{L}_{out}^{rd} + \mathcal{L}_{SA}^{rl}$. The foregrounds are highlighted with red border lines.

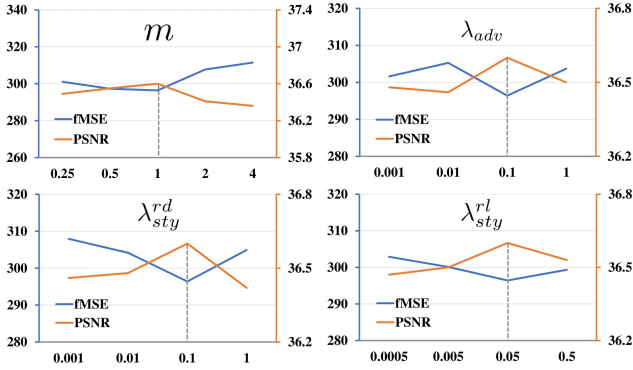


Figure S3: Impact of hyper-parameters, including the margin m in Eqn. 6 and trade-off parameters λ_{adv} , λ_{sty}^{rd} , and λ_{sty}^{rl} in Eqn. 7 in the main text. The results are tested on $\mathcal{D}_{te,n}^{rl}$ and the gray dotted line indicates the default value of each hyper-parameter.

Method	B-T score \uparrow
Input composite	-0.419
iDIH [S5]	0.990
CycleGAN [S7]	0.885
dataset fusion	1.026
Ours	1.404

Table S1: B-T scores of different methods and our CharmNet on 46 real-world composite images with human foregrounds.

S5. Qualitative Analyses on $\mathcal{D}_{te,b}^{rl}$

In Section 5.4 in the main text, we observe that our CharmNet not only boosts the performance on novel category, but also significantly enhances the performance on base categories. Therefore, given a composite real image from $\mathcal{D}_{te,b}^{rl}$, we also provide the harmonization results generated by iDIH [S5] (row 4 in Table 1 in the main text), CycleGAN [S7], dataset fusion, and our CharmNet for comparison. As shown in Figure S6, harmonization results of our CharmNet are more plausible and closer to the ground-truth real images. It could be observed that even if the foreground is not “human”, the foreground style could be well-adapted to the background style, which indicates that the cross-domain style knowledge transfer is also useful for cross-category harmonization. This observation also demonstrates the potential of using rendered im-

egory could boost the performance. Thirdly, when the size of $\mathcal{D}_{tr,n}^{rl}(sub)$ is small, the performance gain brought by $\mathcal{D}_{tr,n}^{rd}$ and our CharmNet is significant, which demonstrates that auxiliary rendered images are especially helpful when the real training set is short of real images from novel categories.

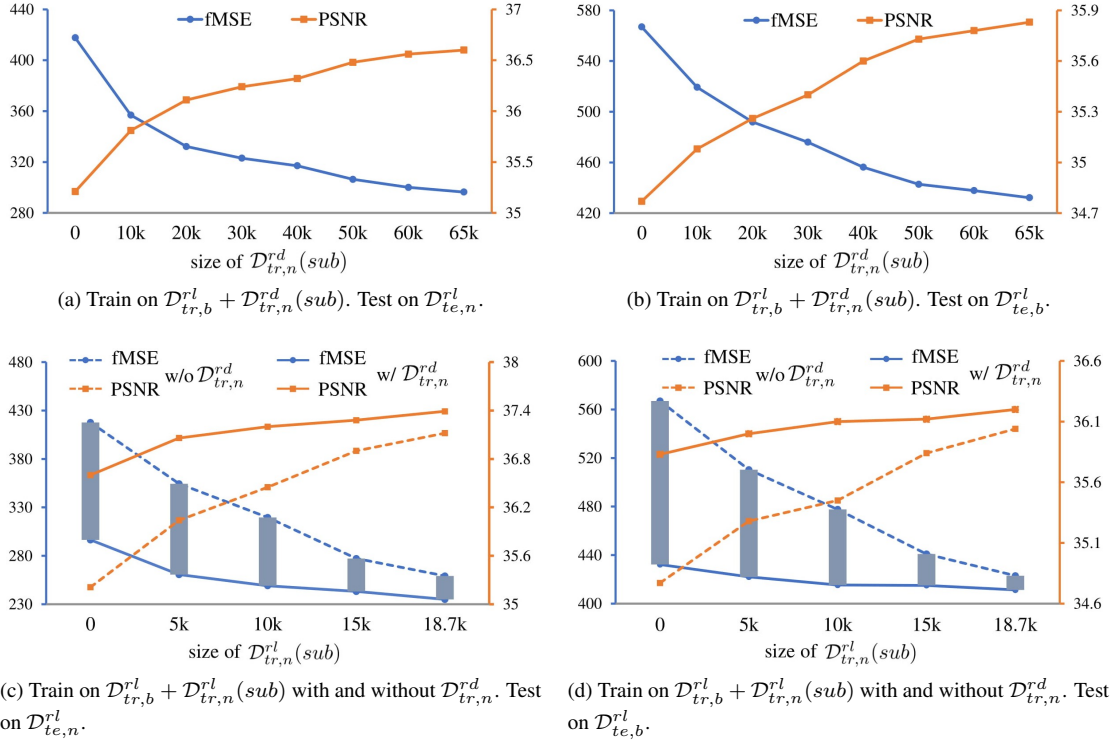


Figure S4: Top row: performance variance when training CharmNet using a subset of $\mathcal{D}^{rd}_{tr,n}$ (i.e., $\mathcal{D}^{rd}_{tr,n}(sub)$) and the full set of $\mathcal{D}^{rl}_{tr,b}$. Sub-figure (a) and (b) show the performance on $\mathcal{D}^{rl}_{te,n}$ and $\mathcal{D}^{rl}_{te,b}$ respectively. Bottom row: performance variance when training CharmNet using a subset of $\mathcal{D}^{rl}_{tr,n}$ (i.e., $\mathcal{D}^{rl}_{tr,n}(sub)$) and the full set of $\mathcal{D}^{rl}_{tr,b}$ with and without the full set of $\mathcal{D}^{rd}_{tr,n}$. Sub-figure (c) and (d) show the performance on $\mathcal{D}^{rl}_{te,n}$ and $\mathcal{D}^{rl}_{te,b}$ respectively.

ages for image harmonization task.

S6. Comparison between Our CharmNet and the Upper Bound

In Table 1 in the main text, our CharmNet outperforms all the domain adaptation baselines and achieves a closer performance to the iDIH [S5] trained with both $\mathcal{D}^{rl}_{tr,n}$ and $\mathcal{D}^{rl}_{tr,b}$, which serves as an upper bound. Therefore, we sample real test images from both $\mathcal{D}^{rl}_{te,n}$ and $\mathcal{D}^{rl}_{te,b}$ and show the ground-truth real images as well as the harmonized results of our CharmNet and the upper bound in Figure S5. It can be observed that our CharmNet could generate harmonious results close to the upper bound for both novel and base categories, which demonstrates the efficacy of our cross-domain harmonization method.

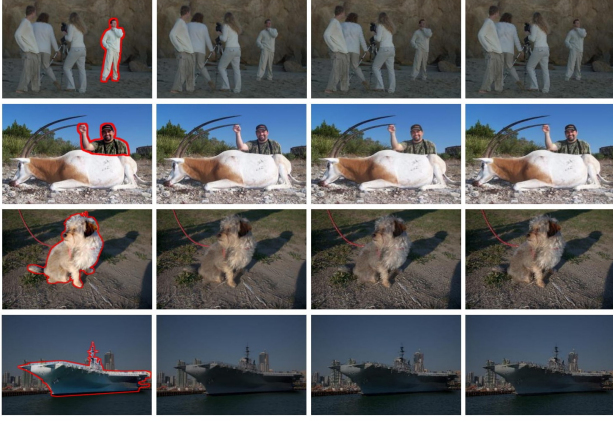
S7. Results on Real-world Composite Images with Human Foregrounds

In practice, image harmonization is expected to tackle with real-world composite images, whose foreground is cut from one image and pasted on another background image. In such a scenario, there are no corresponding ground-truth images, so it is infeasible to evaluate model performance quantitatively. Following

[S2, S3, S6], we conduct user study on 46 real-world composite images with human foregrounds which are selected from 99 real-world composite images released by [S6], and compare the harmonized results generated by iDIH [S5] (row 4 in Table 1 in the main text), CycleGAN [S7], dataset fusion, and our CharmNet using subjective evaluation.

Specifically, for each real-world composite image, we could obtain five images $\{\mathbf{I}_i\}_{i=1}^5$ including itself and four harmonized outputs generated by four above-mentioned methods. Then we can construct image pairs $(\mathbf{I}_i, \mathbf{I}_j)$ by randomly selecting two images from $\{\mathbf{I}_i\}_{i=1}^5$. Based on 46 real-world composite images with human foregrounds, we could construct abundant image pairs for user study. Then we invite 13 users to participate in the study. We ask each user to see one image pair each time and pick out the more harmonious image in the pair. Finally, we collect 5980 pairwise results and employ the Bradley-Terry (B-T) model [S1, S4] to obtain the overall ranking of all methods. As reported in Table S1, our CharmNet achieves the highest B-T score and once again outperforms other baselines.

Besides, we exhibit some example results of real-world composite images with human foregrounds used in our user study. We compare the real-world composite images with harmonization results generated by iDIH [S5] (row 4 in Table 1 in the main text), CycleGAN [S7], dataset fusion, and our CharmNet. As shown in



Input Composite Ground-truth Upper Bound CharmNet

Figure S5: Example results generated by iDIH upper bound and our method. The top two rows are real test images from $\mathcal{D}_{te,n}^r$ and the bottom two rows are real test images from $\mathcal{D}_{te,b}^r$. From left to right, we show the input composite real image, ground-truth real image, as well as the harmonized images generated by the upper bound and our CharmNet. The foregrounds are highlighted with red border lines.

Figure S7, our method is capable of generating more favorable and satisfactory results than other methods.

References

- [S1] Ralph Allan Bradley and Milton E Terry. Rank analysis of incomplete block designs: I. the method of paired comparisons. *Biometrika*, 1952. 4
- [S2] Wenyan Cong, Jianfu Zhang, Li Niu, Liu Liu, Zhixin Ling, Weiyan Li, and Liqing Zhang. DoveNet: Deep image harmonization via domain verification. In *CVPR*, 2020. 4
- [S3] Xiaodong Cun and Chi-Man Pun. Improving the harmony of the composite image by spatial-separated attention module. *IEEE Trans. Image Process.*, 29:4759–4771, 2020. 4
- [S4] Wei-Sheng Lai, Jia-Bin Huang, Zhe Hu, Narendra Ahuja, and Ming-Hsuan Yang. A comparative study for single image blind deblurring. In *CVPR*, 2016. 4
- [S5] Konstantin Sofiiuk, Polina Popenova, and Anton Konushin. Foreground-aware semantic representations for image harmonization. In *WACV*, 2021. 1, 3, 4, 6, 7
- [S6] Yi-Hsuan Tsai, Xiaohui Shen, Zhe Lin, Kalyan Sunkavalli, Xin Lu, and Ming-Hsuan Yang. Deep image harmonization. In *CVPR*, 2017. 4
- [S7] Jun-Yan Zhu, Taesung Park, Phillip Isola, and Alexei A. Efros. Unpaired image-to-image translation using cycle-consistent adversarial networks. In *ICCV*, 2017. 3, 4, 6, 7

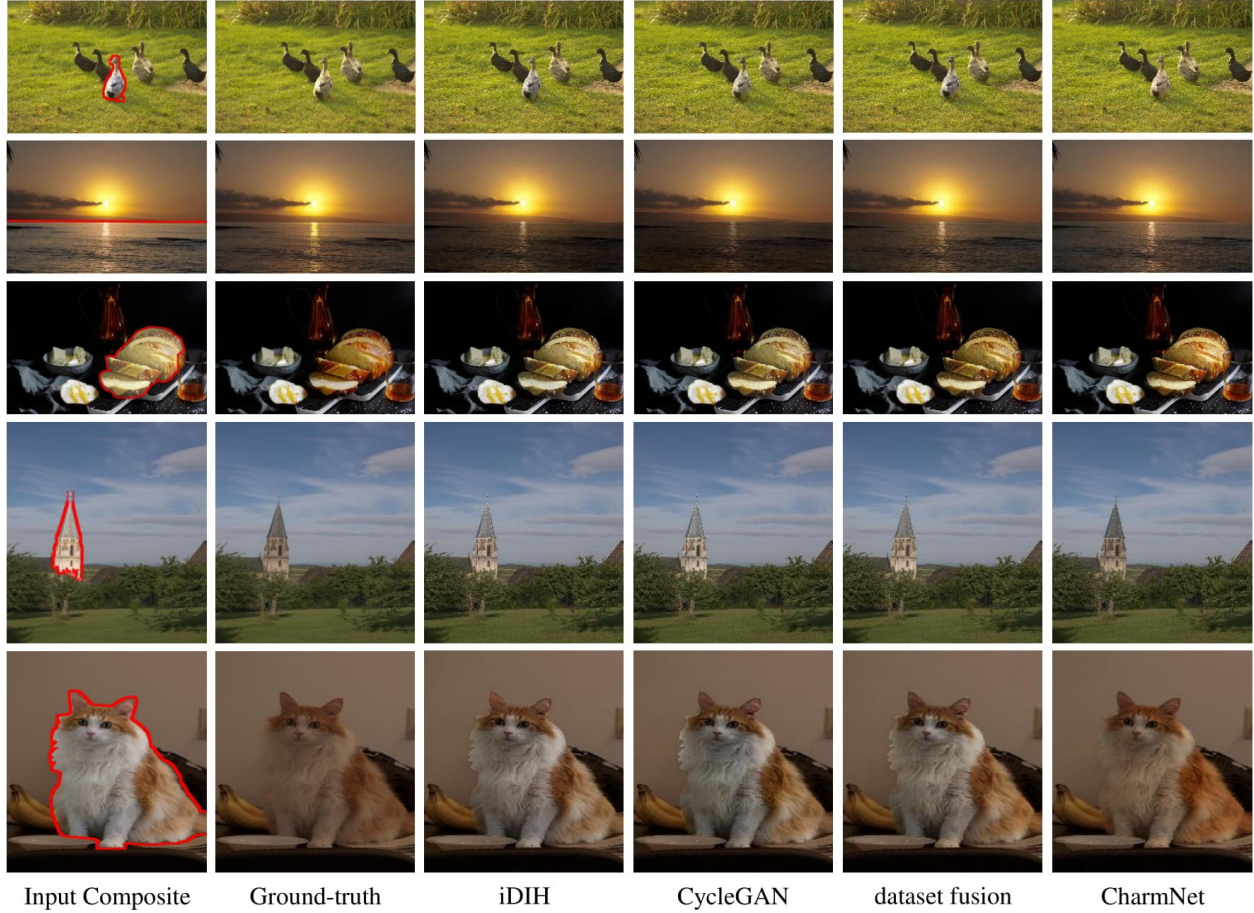


Figure S6: Example results generated by different baselines and our method on $\mathcal{D}_{te,b}^r$. From left to right, we show the input composite real image, ground-truth real image, as well as the harmonized images generated by iDIH [S5] backbone, CycleGAN [S7], dataset fusion, and our CharmNet. The foregrounds are highlighted with red border lines.

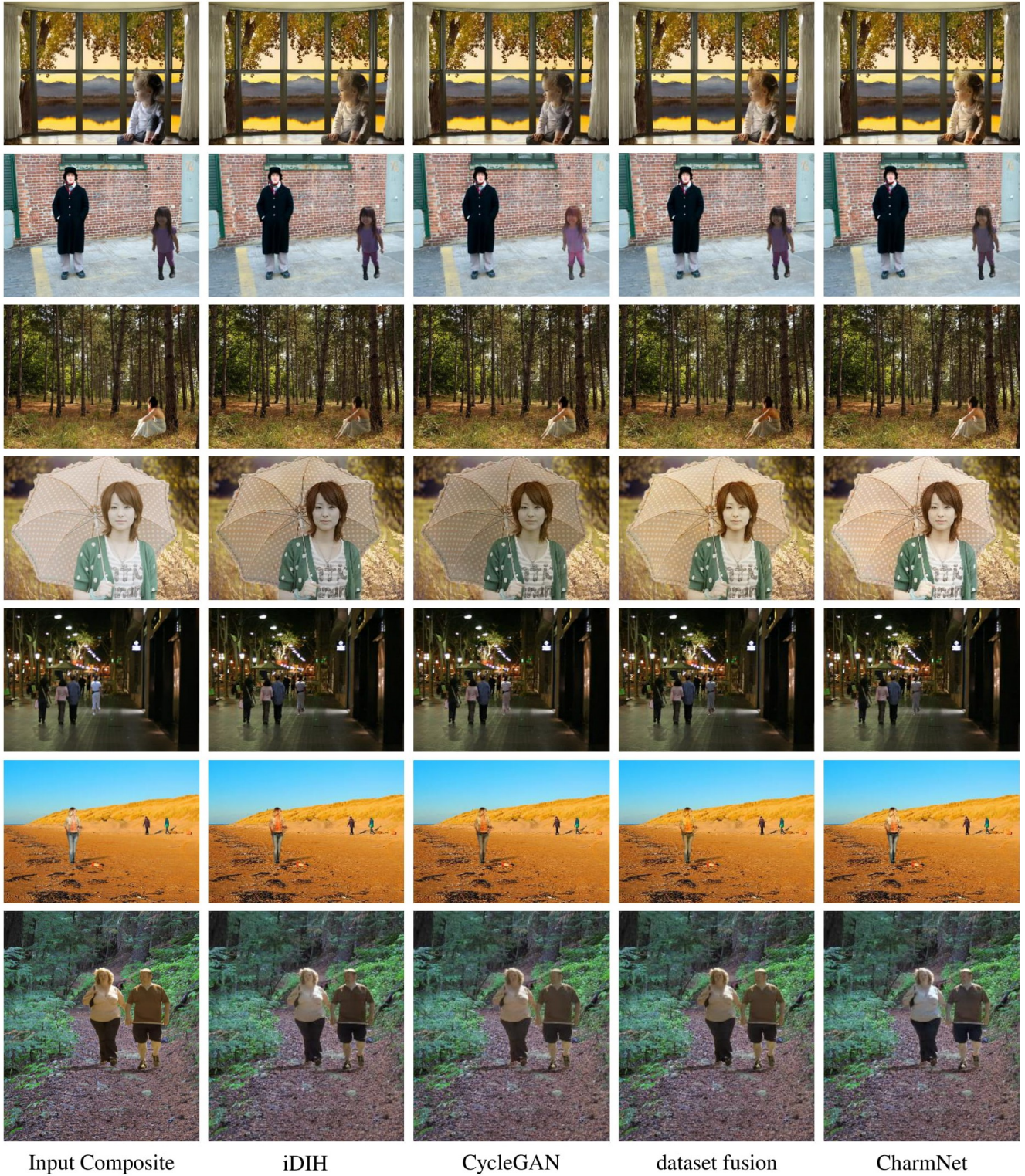


Figure S7: Example results generated by different baselines and our method on real-world composite images with human foregrounds. From left to right, we show the input real-world composite image and the harmonized results generated by iDIH [S5] backbone (row 4 in Table 1 in the main paper), CycleGAN [S7], dataset fusion, and our CharmNet.